C_3 symmetry breaking metal-insulator transitions in a flat band in the half-filled Hubbard model on the decorated honeycomb lattice

H. L. Nourse, Ross H. McKenzie, and B. J. Powell
School of Mathematics and Physics, The University of Queensland, Brisbane, Queensland 4072, Australia

(Received 6 March 2022; accepted 25 April 2022; published 16 May 2022)

We study the single-orbital Hubbard model on the half-filled decorated honeycomb lattice. In the noninteracting theory at half filling the Fermi energy lies within a flat band where strong correlations are enhanced. The lattice is highly frustrated. We find a correlation driven first-order metal-insulator transition to two different insulating ground states—a dimer valence bond solid Mott insulator when intertriangle correlations dominate, and a broken C_3-symmetry antiferromagnet that arises from frustration when intratriangle correlations dominate. The metal-insulator transitions into these two phases have very different characters. The metal-broken C_3 antiferromagnetic transition is driven by spontaneous C_3 symmetry breaking that lifts the topologically required degeneracy at the Fermi energy and opens an energy gap in the quasiparticle spectrum. The metal-dimer valence bond solid transition breaks no symmetries of the Hamiltonian. It is caused by strong correlations renormalizing the electronic structure into a phase that is adiabatically connected to both the trivial band insulator and the ground state of the spin-1/2 Heisenberg model in the relevant parameter regime. Therefore, neither of these metal-insulator transitions can be understood in either the Brinkmann-Rice or Slater paradigms.

DOI: 10.1103/PhysRevB.105.205119

I. INTRODUCTION

There is increasing interest in flat band systems [1]. Strongly correlated physics dominates because all states have the same kinetic energy due to the narrow energy range of the flat band. With the recent discovery of strongly correlated insulators [1–6] and superconductivity [1,7–13] in Moiré flat bands, an open question is whether the superconductivity is linked to strongly correlated physics and/or the flat bands. On the other hand, there is evidence that some Moiré flat bands have superconductivity that is not linked to a correlated insulator [1,11,13]. Answering these open questions in strongly correlated physics [14–20] with these systems is difficult because the physics in many flat band systems are extremely sensitive to material parameters, making reproducibility and experimental probes difficult. Hence, tunable materials that are easy to experimentally probe and that display the above properties are highly sought after.

Many coordination polymers [21] have elaborate lattices with large geometric frustration, which often results in flat bands similar to the kagome lattice [22–33]. Coordination polymers are also often strongly correlated, displaying phenomena such as Mott insulators, Kondo physics [32,33], and unconventional superconductivity [34–36]. Central to our interest is that coordination polymers are highly tunable [37]. Furthermore, coordination polymers often have decorated lattices, and we recently reported that these host a plethora of strongly correlated phenomena as a consequence of the unique lattice and strong electronic correlations [38,39].

Of particular interest is the decorated honeycomb lattice, shown in Fig. 2(a), which hosts many correlated insulators as well as two flat bands. Importantly, the decorated honeycomb lattice has a flat band at half filling, where a Mott insulator occurs [38]. Additionally, a recent study [40] reported unconventional strongly correlated superconductivity in the vicinity of this Mott insulator when doping into the flat band within the framework of Anderson's resonating valence bond solid theory [40]. Hence, decorated lattices in coordination polymers provide a natural path to explore open questions about the connection between strongly correlated insulators, quantum spin liquids, and strongly correlated superconductivity.

In this paper we characterize the ground states of the strongly correlated insulators found in the half-filled Hubbard model on the decorated honeycomb lattice, which is in the vicinity of a flat band. We compare four variational wave functions obtained with mean-field rotationally invariant slave bosons (RISB) that incorporate different spatial correlations depending on the cluster choice: a single site cluster, a dimer cluster that exactly captures short-range intertriangle correlations, and a trimer cluster that exactly captures short-range intratriangle correlations.

The phase diagram of this model is shown in Fig. 1. For large enough Coulomb repulsion there are two different insulating phases that occur via uncommon metal-insulator transitions. For strong intratriangle hopping the frustration of the spins on a triangle causes an insulating state with broken C_3 symmetry (discussed in Sec. IV B). The first-order metal-insulator transition is driven by spontaneous C_3 symmetry breaking, which lifts the topologically required touching of a dispersive band and a flat band at the Fermi energy. For strong intertriangle hopping there is a Mott insulator where spin singlets form along the intertriangle bonds and the ground state is a valence bond solid (VBS) (discussed in Sec. V). In this state no symmetries of the Hamiltonian are broken. The

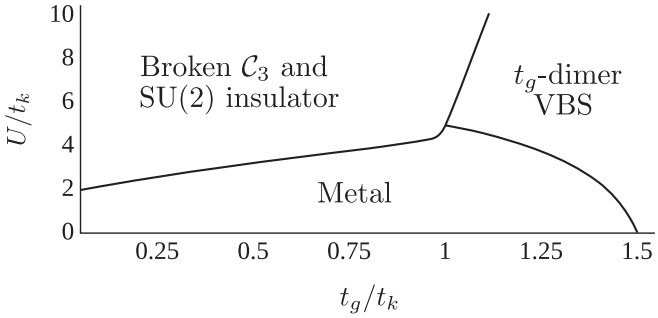

FIG. 1. Phase diagram of the half-filled Hubbard model on the decorated honeycomb lattice (see Fig. 2). Strong electronic correlations drive first-order metal-insulator transitions, the insulating ground state properties of which depend on the ratio of intratriangle hopping t_k and intertriangle hopping t_g. For $t_g/t_k \lesssim 1$ in the insulating state the C_3 symmetry of the triangles is broken. Simultaneously each triangle spin polarizes with antiferromagnetic order between triangles (Fig. 10(a)). For $t_g/t_k \gtrsim 1$ the insulating state is instead a valence bond solid (VBS) that forms spin singlets along the t_g bond (Fig. 10(b)). No symmetries are broken in this state.

first-order Mott metal-insulator transition occurs via a non-symmetry-breaking topological change of the Hamiltonian's electronic structure. This insulating state is adiabatically connected to both the trivial band insulator and the ground state of the spin-1/2 Heisenberg model in the parameter regime where intertriangle interactions are strong. In the large-U limit the ground states compare qualitatively and quantitatively favorably with studies of the Heisenberg model on the decorated honeycomb lattice [41–44] (discussed in Sec. II A).

II. MODEL

The single-orbital Hubbard model on the decorated honeycomb lattice is given by

$$\hat{H} \equiv -t_g \sum_{\langle i\alpha, j\alpha\rangle,\sigma} \hat{c}^\dagger_{i\alpha\sigma}\hat{c}_{j\alpha\sigma} - t_k \sum_{i,\alpha\neq\beta,\sigma} \hat{c}^\dagger_{i\alpha\sigma}\hat{c}_{i\beta\sigma} + U\sum_{i\alpha}\hat{n}_{i\alpha\uparrow}\hat{n}_{i\alpha\downarrow}, \tag{1}$$

where $\hat{c}^{(\dagger)}_{i\alpha\sigma}$ annihilates (creates) an electron with spin σ on site α within triangle i, $\hat{n}_{i\alpha\sigma} \equiv \hat{c}^\dagger_{i\alpha\sigma}\hat{c}_{i\alpha\sigma}$, t_g (t_k) is the hopping parameter between (within) triangles, U is the on-site Coulomb repulsion, and $\langle\cdot\rangle$ denotes only nearest-neighbor hopping. We show the lattice in Fig. 2(a).

In Fig. 2(c) we show the noninteracting limit for $t_g/t_k \leqslant 3/2$. There are a number of exotic features when the decorated honeycomb lattice is at half filling. The Fermi energy lies at a quadratic band touching point with a flat band at $\vec{k} = \vec{0}$ (the Γ point) and the Fermi surface is a single point at Γ with two degenerate states [45,46]. The inclusion of spin orbit coupling opens a gap to a topological quantum spin Hall insulator [47]. At half-filling there is exactly one hole in an infinite peak in the density of states (i.e., one hole shared by the flat-band plus the touching dispersive band at the Γ point).

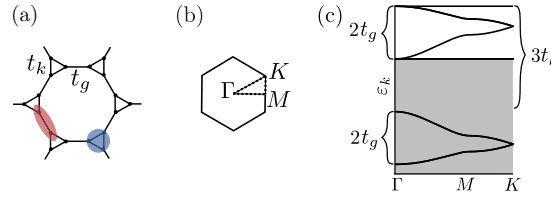

FIG. 2. (a) The decorated honeycomb lattice. The intratriangle hopping parameter is t_k and the intertriangle hopping parameter is t_g. The blue oval denotes the three-site trimer cluster and the red oval denotes the two-site dimer cluster. (b) The Brillouin zone, labeling the points of high symmetry. (c) Noninteracting band structure. When there is on average one electron per site (half filling) the Fermi energy lies at the quadratic band touching point at Γ, with the flat band filled. The gray shaded region denotes the electron filling up to the Fermi energy.

A. Spin-1/2 Heisenberg model

In the limit $U \gg t_g, t_k$ the low-energy effective theory of the half-filled single-orbital Hubbard model is the spin-1/2 Heisenberg model on the decorated honeycomb lattice, given by

$$\hat{H}^{\text{Heis}} \equiv \frac{J_g}{2}\sum_{\langle i\alpha, j\alpha\rangle}\vec{S}_{i\alpha}\cdot\vec{S}_{j\alpha} + \frac{J_k}{2}\sum_{i,\alpha\neq\beta}\vec{S}_{i\alpha}\cdot\vec{S}_{i\beta}, \tag{2}$$

where $J_g = 4t_g^2/U$ is the superexchange along the intertriangle t_g bonds and $J_k = 4t_k^2/U$ along the intratriangle t_k bonds.

Previous exact diagonalization and mean-field studies of the spin-1/2 Heisenberg model [41–43] predict two different VBS states depending on the inter- and intraspin-exchange coupling of a triangle (J_g and J_k, respectively, denoted by J_e and J_t in the cited studies). In the $J_g/J_k \gg 1$ limit (strong coupling between triangles) they predict dimerization along the J_g bond that forms singlets. In the $J_g/J_k \ll 1$ limit (strong coupling within a triangle) they predict a $\sqrt{3}\times\sqrt{3}$ ordered columnar VBS state that forms on a dodecohedron (16-site unit cell) of the decorated honeycomb lattice that breaks the C_3 rotational symmetry of a triangle.

An iPEPS study [44] suggests that the $J_g/J_k \ll 1$ limit (strong coupling within a triangle) is instead a VBS with a six-site unit cell, where singlets form along the J_k bonds, but breaks the C_3 symmetry of a triangle. The study finds that the boundary between the J_g-dimer VBS and the broken C_3 symmetry VBS is $J_g/J_k \sim 0.9$ ($t_g/t_k \sim 0.8$) with threefold ground state degeneracy.

It is remarkable that our mean-field results with the Hubbard model capture many of the features of the proposed ground states of the Heisenberg model, especially the boundary between the t_g-dimer VBS and the broken C_3 symmetry insulator (Fig. 1). As we will show in Sec. V, the t_g-dimer VBS that we find is likely capturing the correct qualitative ground state electronic configuration, with spin singlets along the t_g bonds and large degeneracy. Conversely, the broken C_3 symmetry state that we discuss in Sec. IV B simultaneously has long-range antiferromagnetic order which is not found in the broken C_3 symmetry VBS in [44]. However, our insulating state still has strong short-range antiferromagnetic correlations. The antiferromagnetic state in our paper is likely

a consequence of the mean-field approximation, which does not treat intertriangle correlations exactly in the broken C_3 symmetry state.

III. METHOD

We use mean-field RISB [48–51] to approximate solutions to Eq. (1) using a single-site approximation, two-site dimer clusters [red oval in Fig. 2(a)], and three-site trimer clusters [blue oval in Fig. 2(a)]. For all parameters we compare the energy of each cluster solution to obtain the ground state. At the mean-field level RISB is equivalent to the Gutzillwer approximation [52], which renormalizes a noninteracting wave function by projecting out energetically unfavorable local electronic configurations. Hence, RISB describes the low-energy quasiparticles of a metal and captures metal-insulator transitions.

We implemented mean-field RISB within the TRIQS library [53,54] at zero temperature. The k integrals were evaluated using the linear tetrahedron method [55], and the ground state of a one bath impurity problem was obtained using exact diagonalization with the Arnoldi method in ARPACK-NG [56]. We enforced the C_3 symmetry of a triangle and SU(2) symmetry when investigating the Mott insulator with trimer clusters. We relaxed these symmetries when investigating the broken C_3 symmetry solutions. When investigating the dimer solutions we did not enforce any symmetries. Further details of our formalism and implementation are described in [38,39].

In RISB the physical electron operator is mapped to an enlarged Hilbert space with bosons $\{\hat{\Phi}_{iAn}\}$ and auxiliary fermions $\{\hat{f}_{ia}\}$. The bosons keep track of the 2^{M_i} quasiparticle electronic configurations $\{|n_i\rangle\}$ within each cluster i and relate it to the 2^{M_i} physical electronic configurations $\{|A_i\rangle\}$. Here M_i are the number of sites, orbitals, and spins in cluster i. We restrict our solutions to the set of bosons where the number of auxiliary fermions in state $|n_i\rangle$, denoted N_{in}, is equivalent to the number of physical electrons in state $|A_i\rangle$, denoted N_{iA}.

The physical electron in the enlarged Hilbert space is created by

$$\underline{\hat{c}}^{\dagger}_{i\alpha\sigma} \equiv \sum_{a\sigma'} \hat{\mathcal{R}}^{\sigma'\sigma}_{ia\alpha} \hat{f}^{\dagger}_{ia\sigma'}, \tag{3}$$

with the unitary operator

$$\hat{\mathcal{R}}^{\sigma'\sigma}_{ia\alpha} \equiv \sum_{AB}\sum_{nm} \frac{\langle A_i|\hat{c}^{\dagger}_{i\alpha\sigma}|B_i\rangle\langle n_i|\hat{f}^{\dagger}_{ia\sigma'}|m_i\rangle}{\sqrt{N_{iA}(M_i - N_{iB})}} \hat{\Phi}^{\dagger}_{iAn}\hat{\Phi}_{iBm}, \tag{4}$$

where N_{iA} is the number of electrons in state $|A_i\rangle$. The constraints

$$\sum_{An} \hat{\Phi}^{\dagger}_{iAn}\hat{\Phi}_{iAn} = \hat{1}, \tag{5}$$

$$\sum_{Anm} \langle m_i|\hat{f}^{\dagger}_{ia\sigma}\hat{f}_{ib\sigma'}|n_i\rangle \hat{\Phi}^{\dagger}_{iAn}\hat{\Phi}_{iAm} = \hat{f}^{\dagger}_{ia\sigma}\hat{f}_{ib\sigma'} \tag{6}$$

are used to select the physical states out of the enlarged Hilbert space, where $\hat{1}$ is the identity. The first constraint enforces that the physical states are those where there is exactly one boson on every cluster, and the second constraint ensures that the correct boson is attached to the correct auxiliary fermion electronic configuration. Any operator $\hat{X}_i$ on cluster i can be written quadratically in the bosons, given by

$$\underline{\hat{X}}_i = \sum_{AB} \langle A_i|\hat{X}_i|B_i\rangle \sum_n \hat{\Phi}^{\dagger}_{iAn}\hat{\Phi}_{iAn}. \tag{7}$$

TABLE I. The components of the auxiliary fermion Hamiltonian that corresponds to the renormalized hopping parameters t^*_k and t^*_g for the three different cluster choices. The quasiparticle weight matrix $\boldsymbol{Z} = \boldsymbol{\mathcal{R}}^{\dagger}\boldsymbol{\mathcal{R}}$ renormalizes intercluster hopping, while the correlation potential matrix $\boldsymbol{\lambda}$ gives that renormalized intracluster hopping. We highlight that t^*_g and t^*_k are approximate descriptions because $\boldsymbol{Z}$ is a matrix that may have off-diagonal components. Kotliar-Ruckenstein (KR) refers to a single-site cluster, "Dimer" is a two-site cluster, and "Trimer" is a three-site cluster (see Fig. 2).

Hopping parameter	KR	Dimer	Trimer
t^*_k	$t_k[\boldsymbol{Z}]_{11}$	$t_k[\boldsymbol{Z}]_{11}$	$-[\boldsymbol{\lambda}]_{12}$
t^*_g	$t_g[\boldsymbol{Z}]_{11}$	$-[\boldsymbol{\lambda}]_{12}$	$t_g[\boldsymbol{Z}]_{11}$

At the mean-field level we assume all clusters are equivalent and that the bosons condense to a c number ($\hat{\Phi}_{iAn} \to \phi_{An}$). Under this approximation the auxiliary fermions are described by an effective noninteracting Hamiltonian of quasiparticles, given by

$$\begin{aligned}\hat{H}^{\mathrm{QP}} &\equiv -\sum_{ij}\sum_{\alpha\beta,\sigma}\sum_{ab,\sigma'} [\boldsymbol{\mathcal{R}}]^{\sigma\sigma'}_{a\alpha}[t_{ij}]_{\alpha\beta}[\boldsymbol{\mathcal{R}}^{\dagger}]^{\sigma\sigma''}_{\beta b}\hat{f}^{\dagger}_{ia\sigma'}\hat{f}_{jb\sigma''} \\ &\quad + \sum_{i,ab,\sigma\sigma'} [\boldsymbol{\lambda}]_{ab}\hat{f}^{\dagger}_{ia\sigma}\hat{f}_{ib\sigma'} \\ &= -t^*_g \sum_{\langle ia,ja\rangle,\sigma} \hat{f}^{\dagger}_{ia\sigma}\hat{f}_{ja\sigma} - t^*_k \sum_{i,a\neq b,\sigma} \hat{f}^{\dagger}_{ia\sigma}\hat{f}_{ib\sigma} \\ &\quad + \ldots, \end{aligned} \tag{8}$$

where t^*_g and t^*_k are the renormalized hopping parameters of Eq. (1) and the ellipsis is negligible off-diagonal terms. Metallic solutions of Eq. (8) at zero temperature describe a Landau Fermi liquid with dressed coherent quasiparticles $\{\hat{f}^{\dagger}_{ia\sigma}\}$ that are renormalized by the local interaction U, with the renormalization captured in the mean-field matrices $\boldsymbol{\mathcal{R}}$ and $\boldsymbol{\lambda}$. Table I summarizes how these mean-field matrices relate to the renormalized hopping for different cluster choices.

Hence, we can study the stability of metallic solutions using Eq. (8) from the perspective of band theory with renormalized hopping. Diagonalizing Eq. (8) in reciprocal space gives

$$\hat{H}^{\mathrm{QP}} = \sum_{\vec{k}n} \varepsilon^{\mathrm{QP}}_{\vec{k}n}\hat{\psi}^{\dagger}_{\vec{k}n}\hat{\psi}_{\vec{k}n}, \tag{9}$$

where $\varepsilon^{\mathrm{QP}}_{\vec{k}n}$ is the dispersion of the Landau quasiparticles $\{\hat{\psi}^{\dagger}_{\vec{k}n}\}$ at reciprocal lattice vector $\vec{k}$ and band n. On the other hand, from Eq. (7), the local properties on a cluster in real space can be investigated from the condensed bosons.

A. Metal-insulator transitions in RISB

It is useful to understand how a correlation driven metal-insulator transition is described in the original formulation of Kotliar-Ruckenstein (KR) slave bosons [48], where a Mott

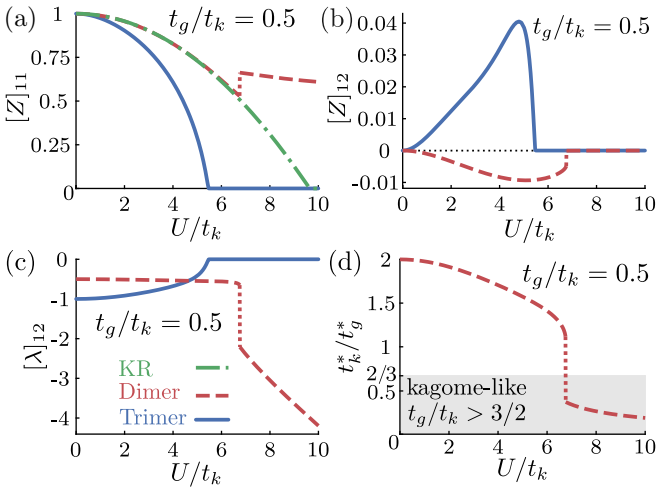

FIG. 3. The quasiparticle weight $\boldsymbol{Z}$ and correlation potential matrix $\boldsymbol{\lambda}$ for $t_g/t_k = 0.5$. We show the KR (single site cluster) solution, the dimer cluster solution, and the trimer cluster solution (see Table I) without allowing any symmetries of the Hamiltonian to break. (a) The diagonal component $[\boldsymbol{Z}]_{11}$ renormalizes the intercluster hopping. In the KR solution the hopping between all sites vanishes at the metal-insulator transition, in the dimer cluster the hopping t_k^* remains finite, and in the trimer cluster hopping between triangles t_g^* vanishes. (b) The off-diagonal components $[\boldsymbol{Z}]_{12}$ of intercluster hopping are small in the correlated metal and vanish at the metal-insulator transition. (c) The off-diagonal component of $[\boldsymbol{\lambda}]_{12}$ renormalizes the intracluster hopping. At the metal-insulator transition in the dimer cluster there is a strong enhancement of t_g^*, and in the trimer cluster intratriangle hopping t_k^* vanishes. (d) Renormalized hopping ratio t_k^*/t_g^*. The metal-insulator transition occurs in the dimer cluster solution by discontinuously opening a gap and changing the bands to the $t_g/t_k > 3/2$ regime where it is a band insulator.

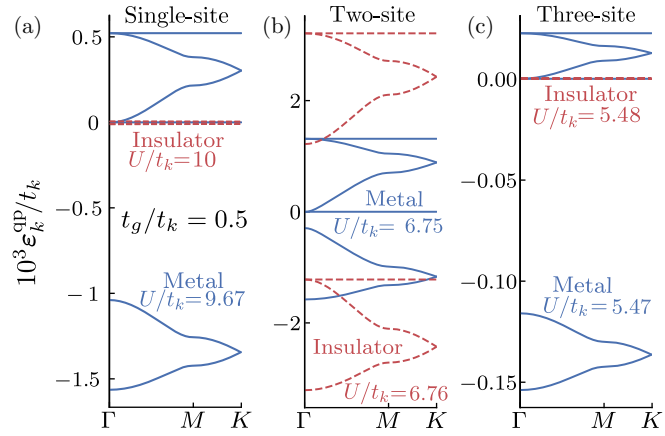

FIG. 4. Renormalized band structure of the KR, dimer cluster, and trimer cluster solutions for $t_g/t_k = 0.5$ without allowing any symmetries of the Hamiltonian to break. The Mott insulator on the half-filled decorated honeycomb lattice is captured differently depending on the cluster choice. In the (a) KR and (c) trimer cluster solutions the bands narrow and become flat at the metal-insulator transition. In contrast, in the (b) dimer cluster solution the bands become kagome-like ($t_k^*/t_g^* < 3/2$) at the metal-insulator transition and a gap opens. The dispersion $\boldsymbol{\varepsilon}_k^{\rm QP}$ denotes the eigenenergies of the quasiparticle Hamiltonian Eq. (9).

insulator (no symmetry breaking) occurs at half filling via the Brinkmann-Rice mechanism [57]. As the metal-insulator transition is approached the quasiparticle bands described by Eq. (9) become renormalized and narrow because intersite hopping is proportional to the quasiparticle weight Z. In this case, both t_k and t_g are renormalized by the same amount (Table I). At the metal-insulator transition the quasiparticle weight vanishes continuously [Fig. 3(a), dot-dashed green line] and the bandwidth of the quasiparticle bands goes to zero [Fig. 4(a)]. In the Brinkmann-Rice insulator the double occupancy vanishes [Fig. 5(a), dot-dashed green line] with a spin-1/2 particle isolated on each site [Fig. 5(b), dot-dashed green line].

Within single-site slave-boson (KR) theory an insulator occurs without breaking a symmetry through the Brinkmann-Rice mechanism, where intercluster charge fluctuations vanish, as can be seen from its equivalence to the Gutzwiller approximation [52]. The only other way for a correlated insulator to occur within KR theory is by breaking a symmetry, such as through the Slater mechanism where spontaneous magnetization occurs.

However, because cluster extensions to RISB are able to couple intracluster physical electronic configurations with other symmetry compatible quasiparticle configurations [see Eq. (4)], the renormalized quasiparticle bands can be shifted and narrowed by differing amounts. Hence, an insulator can occur within RISB without breaking a symmetry that is not through the Brinkmann-Rice mechanism, as has been shown in multiband extensions to the Gutzwiller approximation [58]. In Sec. IV A we discuss a symmetry broken correlated insulator on the half-filled decorated honeycomb lattice, while in Sec. V we discuss a correlated insulator that does not break any symmetries of the Hubbard model and does not occur through the Brinkmann-Rice mechanism.

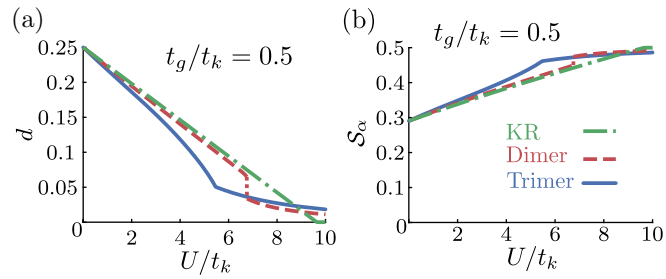

FIG. 5. (a) Double occupancy d and (b) effective spin per site $\mathcal{S}_\alpha$ for $t_g/t_k = 0.5$ without allowing any symmetry of the Hamiltonian to break. In the insulator there is, on average, one electron localized to a site, acting as a spin-1/2 degree of freedom. Only in the two-site and three-site clusters are there intersite charge and spin fluctuations. Double occupancy per site d is given by $d = \sum_{i\alpha}\langle \hat{n}_{i\alpha\uparrow}\hat{n}_{i\alpha\downarrow}\rangle/\mathcal{N}_\nu$, where $\mathcal{N}_\nu$ is the number of sites on the lattice. The effective spin per site is the solution to $\mathcal{S}_\alpha(\mathcal{S}_\alpha+1) = \sum_{i\alpha}\langle \vec{S}_{i\alpha}\cdot\vec{S}_{i\alpha}\rangle/\mathcal{N}_\nu$ where $\vec{S}_{i\alpha} = \frac{1}{2}\sum_{\sigma\sigma'}\hat{c}^\dagger_{i\alpha\sigma}\vec{\tau}_{\sigma\sigma'}\hat{c}_{i\alpha\sigma'}$, and $\vec{\tau}$ is the vector of Pauli matrices.

IV. BROKEN C_3 SYMMETRY ANTIFERROMAGNETIC INSULATOR

In this section we investigate the half-filled decorated honeycomb lattice in the regime where the trimer cluster [Fig. 2(a)] gives the lowest energy. We find that strong electronic correlations drive a Mott metal-insulator transition, the low-energy effective theory of which is the antiferromagnetic spin-1/2 Heisenberg model on the decorated honeycomb lattice. The intratriangle coupling dominates compared to the intertriangle coupling and the spins within a triangle are frustrated. The system further lowers its energy by simultaneously breaking the C_3 symmetry of a triangle and stabilizing long-range antiferromagnet order. We will describe how RISB captures this state.

A. Mott insulator (no spontaneous symmetry breaking)

We first investigate the correlation driven Mott metal-insulator transition where no symmetries of Eq. (1) are broken in order to understand the effects of strong correlations. We enforce the SU(2) and C_3 symmetry of the Hubbard model on the decorated honeycomb lattice. In cluster extensions of mean-field RISB theory the original Hamiltonian Eq. (1) is mapped to a noninteracting one with different renormalized intertriangle t_g^* and intratriangle t_k^* hopping parameters [Eq. (8)]. In the three-site cluster the matrix $\boldsymbol{Z} \equiv \boldsymbol{\mathcal{R}}^\dagger \boldsymbol{\mathcal{R}}$ captures the renormalization of t_g, while the matrix $\boldsymbol{\lambda}$ describes the renormalization of t_k (See Eq. 8 and Table I).

In Fig. 3(a) (solid blue line) we show the renormalization of the intertriangle hopping $t_g^* = t_g[\boldsymbol{Z}]_{11}$ and in Fig. 3(c) (solid blue line) the renormalized intratriangle hopping $t_k^* = -[\boldsymbol{\lambda}]_{12}$ as electronic correlations are increased. Both t_g^* and t_k^* decrease as the metal-insulator transition is approached until the Fermi surface vanishes. In the insulator $t_g^* = t_k^* = 0$. In Fig. 4(c) we show the insulator from the perspective of band theory. Correlations narrow the bands. The upper set of bands, which have primarily E molecular orbital character [38,39], narrows more than the lower set of bands, which have primarily A molecular orbital character. This asymmetrical renormalization is captured by small off-diagonal components of the quasiparticle matrix $\boldsymbol{Z}$, shown in Fig. 3(b) (solid blue line). Regardless, at the metal-insulator transition the bandwidth of the quasiparticle bands vanishes, indicating electrons have become localized. Hence, the metal-insulator transition occurs by the Brinkmann-Rice mechanism.

In Fig. 5(a) (solid blue line) we show the average double occupancy on a site. In Fig. 5(b) (solid blue line) we show the effective spin per site, demonstrating that the localized electrons act as spin-1/2 particles. Even though the renormalized hopping parameters vanish in the insulator ($t_g^* = t_k^* = 0$) there are still intratriangle charge fluctuations. These charge fluctuations are responsible for the dynamical effects in the insulator, such as the superexchange between the spin-1/2 particles.

In Fig. 6(a) (solid blue line) we show the sum of the intratriangle spin exchange between all three sites. In the Mott insulator the sum of the spin exchange approaches the limit of an isolated triangle, signifying antiferromagnetic correlation. Hence, spin singlets between adjacent sites are favored.

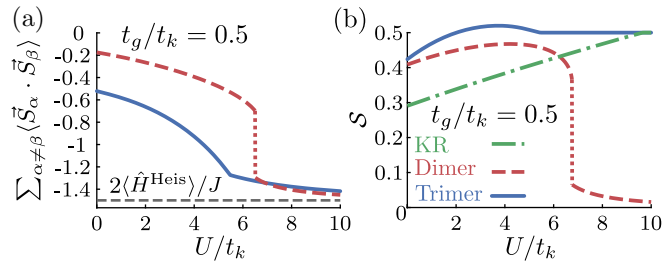

FIG. 6. (a) Sum of the spin-spin correlations within a cluster and (b) total spin $\mathcal{S}$ on a cluster. Spin singlets are formed between sites in the insulator. The insulator in the two-site cluster is a dimer lattice with spin singlets along the intertriangle t_g bonds. In the three-site cluster spin singlets form along the intratriangle t_k bonds. The single-site cluster has no spin exchange between sites because the insulator is adiabatically connected to the atomic limit. $\hat{H}^{\rm Heis}$ is the nearest-neighbor spin-1/2 Heisenberg model [Eq. (2)] on a $\mathcal{N}_c$ ring with antiferromagnetic exchange. The effective spin per cluster is the solution to $\mathcal{S}(\mathcal{S}+1) = \sum_i \langle \vec{S}_i \cdot \vec{S}_i \rangle \mathcal{N}_c/\mathcal{N}_v$, where $\vec{S}_i = \sum_\alpha \vec{S}_{i\alpha}$, and $\mathcal{N}_c$ is the number of sites within a cluster.

However, as shown in Fig. 6(b) (solid blue line), because of the frustration on a triangle spin singlets form along the intratriangle t_k bonds with on average half a spin left over. In Sec. IV B we will show that this frustration causes the C_3 symmetry of a triangle to break and drives a metal-insulator transition. We highlight that in the true ground state there will also be a weaker antiferromagnetic spin exchange across the t_g bonds of the lattice, but our results only capture this at the mean-field level in the three-site cluster approximation.

The resulting picture is a localized electron on each site behaving as a spin-1/2 particle, with antiferromagnetic spin exchange between sites generated from virtual charge excitations of doubly occupied sites. That is, the Mott insulator is described by the spin-1/2 Heisenberg model [Eq. (2)] on the decorated honeycomb lattice, with short-range antiferromagnetic correlations within a triangle stabilizing the insulator.

B. Spontaneously broken C_3 symmetry insulator

We now relax the constraints to allow the SU(2) and C_3 symmetries of Eq. (1) to break. We find that there is a first-order metal-insulator transition where in the insulator each triangle spin polarizes with antiferromagnetic order between triangles and different renormalized hopping t_k^* across the three bonds within a triangle, indicating that the C_3 symmetry of a triangle has broken. The metal-insulator transition is driven by spontaneous C_3 symmetry breaking.

In Fig. 7(a) we show the staggered magnetization between triangles, given by

$$m_s \equiv \frac{3}{\mathcal{N}_v} \sum_i \left| (-1)^{\eta(i)} \langle \hat{S}_i^z \rangle \right|, \tag{10}$$

where $\eta(i) = 0\,(1)$ for the two inequivalent triangles. A finite m_s signifies antiferromagnetic order between triangles due to spin polarization on a triangle and breaks the SU(2) symmetry of the Hamiltonian. There is a discontinuous phase transition to a magnetic state that occurs by increasing U/t_k. The state has on average a leftover polarized spin-1/2 on each triangle

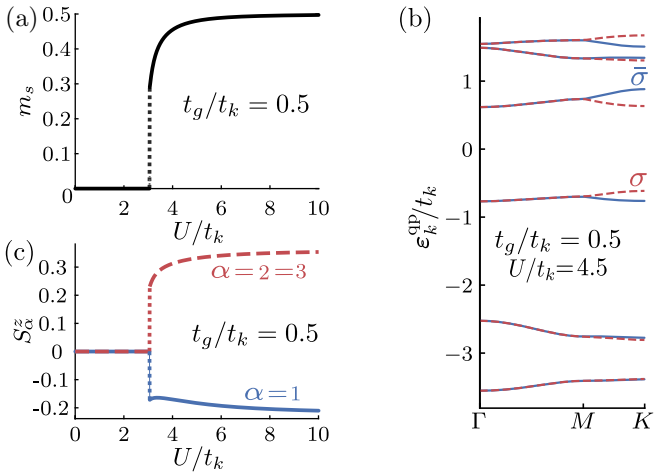

FIG. 7. (a) The staggered magnetization m_s [Eq. (10)]. There is a discontinuous metal-insulator transition to an antiferromagnetic state, where the magnetic order is between triangles. (b) The quasiparticle bands [Eq. (8)]. The insulator occurs by spontaneously breaking the C_3 rotational symmetry of a triangle and opening a gap at $\vec{k} = \vec{0}$ (the Γ point). (c) The average z component of spin for each site in a triangle S_α^z. $S_\alpha^z = \sum_i (-1)^{\eta(i)} \sum_{\sigma\sigma'} \langle \hat{n}_{i\alpha\uparrow} - \hat{n}_{i\alpha\downarrow} \rangle / \mathcal{N}_v$. The majority (minority) spin is labeled by σ ($\bar{\sigma}$).

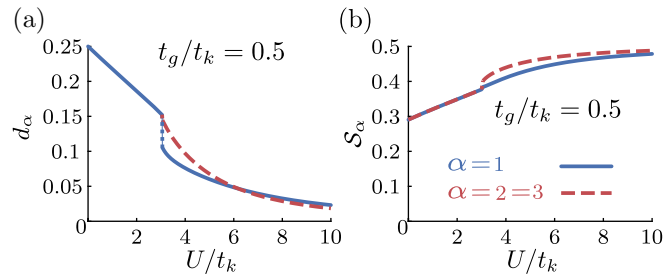

FIG. 8. (a) Double occupancy on each site d_α and (b) total spin on each site $\mathcal{S}_\alpha$ for the broken C_3 symmetry insulator for $t_g/t_k = 0.5$. Increasing correlation causes electrons to localize on each site, with on average one electron per site with small charge fluctuations. For large U/t_k and in the insulator there is on average one electron per site acting as a spin-1/2 degree of freedom.

($m_s \to 1/2$) for large U. The antiferromagnetic order lifts the degeneracy of the high symmetry point K (the Dirac point) in the quasiparticle spectrum because inversion about the t_g bond is broken [39]. Correlation driven antiferromagnetism that is responsible for opening an energy gap in the quasiparticle spectrum is known as the Slater mechanism [59]. However, the Fermi energy is not at the Dirac points and hence the Slater mechanism, driven by antiferromagnetism, is not sufficient to drive the metal-insulator transition.

As was previously discussed in Sec. IV A for solutions with no broken symmetries, the Mott insulator will favor the formation of spin singlets along the t_g bonds of the lattice. Our calculations do not capture the spin exchange across the t_g bond exactly, the mean-field solution instead describes a broken symmetry state of the singlet, resulting in long-range antiferromagnetic order of the triangles. This suggests that in the true ground state SU(2) may not break and there is instead a singlet along the t_g bond.

Instead, the metal-insulator transition is driven by additionally spontaneously breaking the C_3 symmetry of a triangle. In Fig. 7(c) we show the average z component of the spin per site on a triangle. We find that there is a different spin polarization S_α^z on each site. Hence, each site is not equivalent and the 120° rotational symmetry is broken. Note that this rules out, e.g., 120° order of the spins on a triangle.

The broken C_3 symmetry is accompanied by opening a gap via lifting the twofold degeneracy at the Γ point ($\vec{k} = \vec{0}$) where the flat band touches the dispersive band. In Fig. 7(b) we show the quasiparticle spectrum [Eq. (9)] of the magnetic insulator. In the metallic state the Fermi energy is at the quadratic band touching point at $\vec{k} = \vec{0}$. There is one hole per spin flavor shared between the states of the flat band and the state of the dispersive band that touches at the Γ point. Because the degeneracy at the Γ point is a consequence of the topology of the lattice [45,46], the only way to break the degeneracy and open a gap in the quasiparticle spectrum is by breaking symmetries of the Hamiltonian. Spontaneously breaking C_3 symmetry lifts the topological requirement that the flat band touches the dispersive band and allows a gap to open at the Fermi energy. Consequently, in the insulator all quasiparticle bands become isolated from each other, narrow, and highly localized. We are not aware of other examples where a metal-insulator transition occurs via the topologically required degeneracy at the Fermi energy being lifted by strong electronic correlations.

Similarly to the solutions presented in Sec. IV A, where no symmetries break, charge fluctuations are heavily suppressed in the broken C_3 symmetry insulator because of strong correlations. In Fig. 8(a) we show the double occupancy on a site. Electrons become localized to each site and form an effective spin-1/2 degree of freedom [Fig. 8(b)] with small charge fluctuations.

There are two major differences compared to the Mott insulator with no broken symmetries. First, the spin-1/2 degree of freedom on each site polarizes [Fig. 7(b)] and the insulator is stabilized by long-range antiferromagnetic correlations, giving antiferromagnetic order between triangles. Second, the equally weighted singlet formation along the t_k bonds within a triangle is broken because of the broken C_3 symmetry. In Fig. 9(a) we show the spin-spin correlations between the sites within a triangle. In the Mott insulator with no broken symmetries frustration makes it difficult to satisfy spin singlets between neighboring sites within a triangle. In the broken C_3 symmetry insulator the state compromises by polarizing and only antialigning two of the sites, with a ferromagnetic spin coupling to the leftover site. We show the short-range spin correlations schematically in Fig. 10(a). As shown in Fig. 9(b), the sum of the energy contribution from the spin correlations on a triangle approaches those found in the spin-1/2 Heisenberg model on a three-site ring.

In Fig. 11 we show a schematic of the magnetic order on the lattice. In our results we showed the representative state shown in Fig. 11(a), but there are other spin configurations that are degenerate. There are a total of 18 states within a unit cell that have the same energy. However, the macroscopic degeneracy is likely a consequence of the three-site cluster.

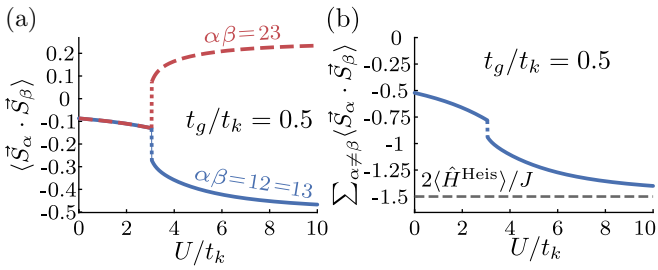

FIG. 9. (a) Spin-spin correlation between sites within a triangle for the broken C_3 symmetry insulator for $t_g/t_k = 0.5$. (b) The sum of the spin correlations between sites within a cluster approaches the correlations in the ground state of the spin-1/2 Heisenberg model on an $\mathcal{N}_c$ ring [see Eq. (2)], where $\mathcal{N}_c$ is the number of sites within a cluster. The spin operator on site α of cluster i is given by $\vec{S}_{i\alpha} = \frac{1}{2}\sum_{\sigma\sigma'}\hat{c}^\dagger_{i\alpha\sigma}\vec{\tau}_{\sigma\sigma'}\hat{c}_{i\alpha\sigma'}$ where $\vec{\tau}$ is the vector of Pauli matrices.

Correlations are treated exactly along the t_k bonds, while correlations along the t_g bonds are only treated at the mean-field level. Therefore, the superexchange along the t_g bond is not captured faithfully, where it is expected to favor singlet correlations. iPEPS calculations [44], which we discussed in Sec. II A, suggest that instead of magnetic order there may be three singlets on a triangle with differing strength. It is likely that our calculations do not capture this state because of the finite cluster size, and hence instead the spins polarize and the SU(2) symmetry of the Hamiltonian breaks.

V. t_g-DIMER VALENCE BOND SOLID MOTT INSULATOR

In this section we investigate the effect of strong correlations with a dimer cluster [red oval in Fig. 2(a)] along the t_g bonds, treating the correlations along the t_g bonds exactly and the correlations along the t_k bonds at the mean-field level. We find that there is a true first-order Mott (no broken symmetry of the Hamiltonian) metal-insulator transition to a state that favors spin singlets along the t_g bonds, which we call a t_g-dimer VBS. However, the mechanism is very different from either the Brinkmann-Rice or Slater mechanism. The mechanism that causes the Mott metal-insulator transition is similar to one

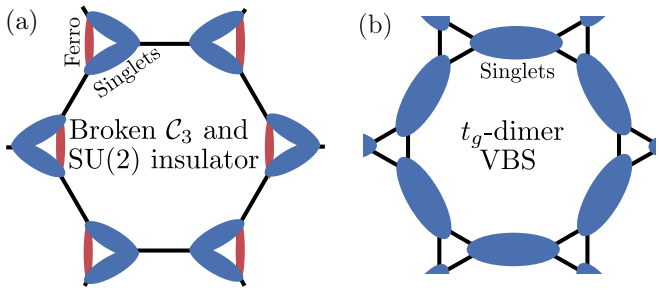

FIG. 10. Schematic representation of the singlet formation in the insulators. (a) In the broken C_3 symmetry insulator there are singlets along two of the t_k bonds of a triangle, with the third bond a weaker $S^z = \pm 1$ triplet. (b) In the t_g-dimer VBS singlets form along the t_g bonds. The blue ovals represent singlets and the red ovals represent ferromagnetic correlations. Compare with Fig. 9(a).

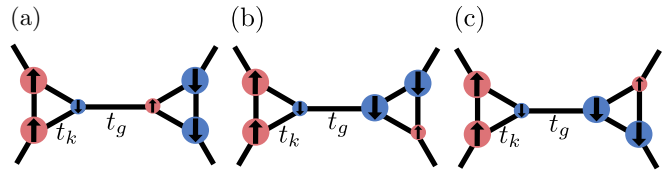

FIG. 11. Schematic representation of the degenerate spin configurations of a site in the broken C_3 insulator. There are six other states by permuting the configurations on one of the triangles, and another nine states from flipping the spin on each site. There are in total 18 degenerate states.

that occurs in the Hubbard model on the dimer lattice model [58].

In Fig. 3 (red dashed line) we show the renormalization of the hopping parameters as U is increased for the bare hopping ratio $t_g/t_k = 0.5$. At $U = 0$ the system is metallic with the Fermi energy at the quadratic band touching point at $\vec{k} = \vec{0}$ (the Γ point). At a critical U_c there is a discontinuous change of the renormalized hopping parameters t_k^*/t_g^* to the $t_g/t_k > 3/2$ regime. At $U = 0$ and $t_g/t_k > 3/2$ the system is a band insulator. Electronic correlations drive a metal-insulator transition at U_c by restructuring the electronic structure into the band insulator regime. The resulting insulator is adiabatically connected to the trivial band insulator, and the low-energy excitations remain coherent quasiparticles. Unlike the broken C_3 symmetry insulator, the t_g-dimer VBS remains quantum disordered and does not break any symmetries of the Hamiltonian. Instead, the insulator occurs from a symmetry compatible topological change of the Hamiltonian, as is shown in the quasiparticle band structure of Fig. 4(b).

In Fig. 5(a) (red dashed line) we show the double occupancy per site. Strong electronic correlations suppress charge fluctuations. In the insulator the charge fluctuations become small but do not vanish. Because the t_g-dimer VBS does not occur by the Brinkmann-Rice mechanism, there are still interdimer charge fluctuations. In Fig. 5(b) (red dashed line) we show the effective spin per site, and in Fig. 6(b) (red dashed line) we show the effective spin per dimer. In the insulator there is, on average, one electron localized to each site acting as a spin-1/2 degree of freedom ($\mathcal{S}_\alpha \to 1/2$) with nearest-neighbor antiferromagnetic spin exchange. Hence, a spin singlet forms along the t_g bond ($\mathcal{S} \to 0$). The resulting picture of the insulator is a VBS with singlets along the t_g bonds, which we schematically show in Fig. 10(b).

VI. BOUNDARY BETWEEN BROKEN C_3 SYMMETRY INSULATOR AND t_g-DIMER VBS

In the phase diagram shown in Fig. 1 the t_g-dimer VBS occurs for $t_g/t_k \gtrsim 1$ for a sufficiently large U/t_k. As we have demonstrated, in the half-filled Hubbard model on the decorated honeycomb lattice [Eq. (1)] a Mott metal-insulator transition occurs, the low-energy effective theory of which is the spin-1/2 Heisenberg model [Eq. (2)]. An exact solution to the Hubbard model will correctly capture the superexchange between sites. However, within RISB and the clusters we

choose, the superexchanges along the t_g and t_k bonds are not treated on an equal footing.

We can understand the boundary in Fig. 1 by estimating whether capturing correlations along the t_g or t_k bond is a better representation in the insulating phase by considering the energies of the spin-1/2 Heisenberg model on isolated two- and three-site rings. The ground state energy for an isolated dimer is $\langle \hat{H}^{\text{Heis}} \rangle / J_k = -3/4$ and for an isolated triangle is $\langle \hat{H}^{\text{Heis}} \rangle / J_t = -3/4$. Defining $\mathcal{N}_g \equiv \mathcal{N}_v/2$ and $\mathcal{N}_k \equiv \mathcal{N}_v/3$ as the number of two-site and three-site rings on the decorated honeycomb lattice, respectively, an estimation of the ground state energies of the uncoupled clusters of the spin-1/2 Heisenberg model is given by

$$E_g = -\frac{3}{4}\mathcal{N}_g J_g = -\frac{3}{8}\mathcal{N}_v \frac{4t_g^2}{U},$$
$$E_k = -\frac{3}{4}\mathcal{N}_k J_k = -\frac{1}{4}\mathcal{N}_v \frac{4t_k^2}{U}. \tag{11}$$

The energies are equal ($E_g = E_k$) when

$$\frac{3}{8}t_g^2 = \frac{1}{4}t_k^2$$
$$\Rightarrow \frac{t_g}{t_k} = \sqrt{\frac{2}{3}} \sim 0.816. \tag{12}$$

The boundary occurs because for $t_g/t_k \gtrsim 0.8$ the system gains more energy by forming singlets along the t_g bond, while for $t_g/t_k \lesssim 0.8$ there is a larger energy gain by forming singlets along the t_k bond. We find the same boundary in our solutions for the Hubbard model where there are no spontaneously broken symmetries. However, as shown in Fig. 1, the system can lower its energy further by breaking the C_3 symmetry of a triangle, which extends the trimerized phase to a larger t_g/t_k, and the boundary becomes a function of U/t_k.

VII. CONCLUSION

A broken C_3 symmetry insulator and a t_g-dimer VBS occurs from strong electronic correlations on the half-filled Hubbard model on the decorated honeycomb lattice at zero temperature. The metal-to-broken C_3 symmetry insulator occurs via the lifting of the topologically required degeneracy at the Γ point and opens an energy gap at the Fermi energy. It is accompanied by long-range antiferromagnetic order between triangles. The t_g-dimer VBS is a Mott insulator where there are no broken symmetries, and is adiabatically connected to both the trivial band insulator and the ground state of the spin-1/2 Heisenberg model in the regime where intertriangle spin exchange dominates. The ground states found in our electronic mean-field study show remarkable similarities to quantum disordered states in spin models on the decorated honeycomb lattice [41–44].

Importantly, the insulating states we find occur at half filling of a flat band, where strong correlations are typically enhanced. With the recent prediction of unconventional superconductivity on the decorated honeycomb lattice near half filling [40], there is an open question about the connection between the strongly correlated insulator found in our paper and unconventional superconductivity. A useful direction to explore this connection may be in coordination complexes and polymers where the decorated honeycomb lattice is often found [22–33].

ACKNOWLEDGMENT

This work was supported by the Australian Research Council through Grant No. DP181006201.

[1] L. Balents, C. R. Dean, D. K. Efetov, and A. F. Young, Nat. Phys. **16**, 725 (2020).
[2] K. Kim, A. DaSilva, S. Huang, B. Fallahazad, S. Larentis, T. Taniguchi, K. Watanabe, B. J. LeRoy, A. H. MacDonald, and E. Tutuc, Proc. Natl. Acad. Sci. USA **114**, 3364 (2017).
[3] Y. Cao, V. Fatemi, A. Demir, S. Fang, S. L. Tomarken, J. Y. Luo, J. D. Sanchez-Yamagishi, K. Watanabe, T. Taniguchi, E. Kaxiras, R. C. Ashoori, and P. Jarillo-Herrero, Nature (London) **556**, 80 (2018).
[4] G. Chen, L. Jiang, S. Wu, B. Lyu, H. Li, B. L. Chittari, K. Watanabe, T. Taniguchi, Z. Shi, J. Jung, Y. Zhang, and F. Wang, Nat. Phys. **15**, 237 (2019).
[5] Y. Choi, J. Kemmer, Y. Peng, A. Thomson, H. Arora, R. Polski, Y. Zhang, H. Ren, J. Alicea, G. Refael, F. von Oppen, K. Watanabe, T. Taniguchi, and S. Nadj-Perge, Nat. Phys. **15**, 1174 (2019).
[6] Y. Tang, L. Li, T. Li, Y. Xu, S. Liu, K. Barmak, K. Watanabe, T. Taniguchi, A. H. MacDonald, J. Shan, and K. F. Mak, Nature (London) **579**, 353 (2020).
[7] Y. Cao, V. Fatemi, S. Fang, K. Watanabe, T. Taniguchi, E. Kaxiras, and P. Jarillo-Herrero, Nature (London) **556**, 43 (2018).
[8] M. Yankowitz, S. Chen, H. Polshyn, Y. Zhang, K. Watanabe, T. Taniguchi, D. Graf, A. F. Young, and C. R. Dean, Science **363**, 1059 (2019).
[9] X. Lu, P. Stepanov, W. Yang, M. Xie, M. A. Aamir, I. Das, C. Urgell, K. Watanabe, T. Taniguchi, G. Zhang, A. Bachtold, A. H. MacDonald, and D. K. Efetov, Nature (London) **574**, 653 (2019).
[10] G. Chen, A. L. Sharpe, P. Gallagher, I. T. Rosen, E. J. Fox, L. Jiang, B. Lyu, H. Li, K. Watanabe, T. Taniguchi, J. Jung, Z. Shi, D. Goldhaber-Gordon, Y. Zhang, and F. Wang, Nature (London) **572**, 215 (2019).
[11] P. Stepanov, I. Das, X. Lu, A. Fahimniya, K. Watanabe, T. Taniguchi, F. H. L. Koppens, J. Lischner, L. Levitov, and D. K. Efetov, Nature (London) **583**, 375 (2020).
[12] C. Emilio, W. Qiyue, K. Ryan, C. Shi, T. Haidong, L. Rui, T. Son, W. Kenji, T. Takashi, Z. Fan, B. Marc, and L. C. Ning, Sci. Adv. **5**, eaaw9770 (2022).
[13] H. S. Arora, R. Polski, Y. Zhang, A. Thomson, Y. Choi, H. Kim, Z. Lin, I. Z. Wilson, X. Xu, J.-H. Chu, K. Watanabe, T. Taniguchi, J. Alicea, and S. Nadj-Perge, Nature (London) **583**, 379 (2020).
[14] E. Dagotto, Rev. Mod. Phys. **66**, 763 (1994).

[15] M. Imada, A. Fujimori, and Y. Tokura, Rev. Mod. Phys. **70**, 1039 (1998).
[16] J. Orenstein and A. J. Millis, Science **288**, 468 (2000).
[17] P. A. Lee, N. Nagaosa, and X.-G. Wen, Rev. Mod. Phys. **78**, 17 (2006).
[18] D. J. Scalapino, Rev. Mod. Phys. **84**, 1383 (2012).
[19] E. Fradkin, S. A. Kivelson, and J. M. Tranquada, Rev. Mod. Phys. **87**, 457 (2015).
[20] B. Keimer, S. A. Kivelson, M. R. Norman, S. Uchida, and J. Zaanen, Nature (London) **518**, 179 (2015).
[21] S. R. Batten, N. R. Champness, X.-M. Chen, J. Garcia-Martinez, S. Kitagawa, L. Öhrström, M. O'Keeffe, M. P. Suh, and J. Reedijk, Pure Appl. Chem. **85**, 1715 (2013).
[22] R. Murase, C. F. Leong, and D. M. D'Alessandro, Inorg. Chem. **56**, 14373 (2017).
[23] R. Murase, B. F. Abrahams, D. M. D'Alessandro, C. G. Davies, T. A. Hudson, G. N. L. Jameson, B. Moubaraki, K. S. Murray, R. Robson, and A. L. Sutton, Inorg. Chem. **56**, 9025 (2017).
[24] C. J. Kingsbury, B. F. Abrahams, D. M. D'Alessandro, T. A. Hudson, R. Murase, R. Robson, and K. F. White, Cryst. Growth Des. **17**, 1465 (2017).
[25] I.-R. Jeon, B. Negru, R. P. Van Duyne, and T. D. Harris, J. Am. Chem. Soc. **137**, 15699 (2015).
[26] L. E. Darago, M. L. Aubrey, C. J. Yu, M. I. Gonzalez, and J. R. Long, J. Am. Chem. Soc. **137**, 15703 (2015).
[27] J. A. DeGayner, I.-R. Jeon, L. Sun, M. Dinc, and T. D. Harris, J. Am. Chem. Soc. **139**, 4175 (2017).
[28] L. M. Henling and R. E. Marsh, Acta Crystallogr. Sect. C **70**, 834 (2014).
[29] K. M. Henline, C. Wang, R. D. Pike, J. C. Ahern, B. Sousa, H. H. Patterson, A. T. Kerr, and C. L. Cahill, Cryst. Growth Des. **14**, 1449 (2014).
[30] R. A. Polunin, V. N. Dorofeeva, A. E. Baranchikov, V. K. Ivanov, K. S. Gavrilenko, M. A. Kiskin, I. L. Eremenko, V. M. Novotortsev, and S. V. Kolotilov, Russ. J. Coord. Chem. **41**, 353 (2015).
[31] M. J. Kalmutzki, N. Hanikel, and O. M. Yaghi, Sci. Adv. **4**, eaat9180 (2018).
[32] W. Jiang, Z. Liu, J.-W. Mei, B. Cui, and F. Liu, Nanoscale **11**, 955 (2019).
[33] D. Kumar, J. Hellerstedt, B. Field, B. Lowe, Y. Yin, N. V. Medhekar, and A. Schiffrin, Adv. Funct. Mater **31**, 2106474 (2021).
[34] X. Zhang, Y. Zhou, B. Cui, M. Zhao, and F. Liu, Nano Lett. **17**, 6166 (2017).
[35] X. Huang, S. Zhang, L. Liu, L. Yu, G. Chen, W. Xu, and D. Zhu, Angew. Chem. Int. Ed. **57**, 146 (2018).
[36] T. Takenaka, K. Ishihara, M. Roppongi, Y. Miao, Y. Mizukami, T. Makita, J. Tsurumi, S. Watanabe, J. Takeya, M. Yamashita, K. Torizuka, Y. Uwatoko, T. Sasaki, X. Huang, W. Xu, D. Zhu, N. Su, J.-G. Cheng, T. Shibauchi, and K. Hashimoto, Sci. Adv. **7**, eabf3996 (2021).
[37] O. M. Yaghi, J. Am. Chem. Soc. **138**, 15507 (2016).
[38] H. L. Nourse, R. H. McKenzie, and B. J. Powell, Phys. Rev. B **103**, L081114 (2021).
[39] H. L. Nourse, R. H. McKenzie, and B. J. Powell, Phys. Rev. B **104**, 075104 (2021).
[40] J. Merino, M. F. López, and B. J. Powell, Phys. Rev. B **103**, 094517 (2021).
[41] J. Richter, J. Schulenburg, A. Honecker, and D. Schmalfuß, Phys. Rev. B **70**, 174454 (2004).
[42] G. Misguich and P. Sindzingre, J. Phys.: Condens. Matter **19**, 145202 (2007).
[43] B.-J. Yang, A. Paramekanti, and Y. B. Kim, Phys. Rev. B **81**, 134418 (2010).
[44] S. S. Jahromi and R. Orús, Phys. Rev. B **98**, 155108 (2018).
[45] D. L. Bergman, C. Wu, and L. Balents, Phys. Rev. B **78**, 125104 (2008).
[46] A. C. Jacko, C. Janani, K. Koepernik, and B. J. Powell, Phys. Rev. B **91**, 125140 (2015).
[47] A. Rüegg, J. Wen, and G. A. Fiete, Phys. Rev. B **81**, 205115 (2010).
[48] G. Kotliar and A. E. Ruckenstein, Phys. Rev. Lett. **57**, 1362 (1986).
[49] F. Lechermann, A. Georges, G. Kotliar, and O. Parcollet, Phys. Rev. B **76**, 155102 (2007).
[50] N. Lanatà, Y. Yao, C.-Z. Wang, K.-M. Ho, and G. Kotliar, Phys. Rev. X **5**, 011008 (2015).
[51] N. Lanatà, Y. Yao, X. Deng, V. Dobrosavljević, and G. Kotliar, Phys. Rev. Lett. **118**, 126401 (2017).
[52] J. Bünemann and F. Gebhard, Phys. Rev. B **76**, 193104 (2007).
[53] O. Parcollet, M. Ferrero, T. Ayral, H. Hafermann, I. Krivenko, L. Messio, and P. Seth, Comput. Phys. Commun. **196**, 398 (2015).
[54] P. Seth, I. Krivenko, M. Ferrero, and O. Parcollet, Comput. Phys. Commun. **200**, 274 (2016).
[55] P. E. Blöchl, O. Jepsen, and O. K. Andersen, Phys. Rev. B **49**, 16223 (1994).
[56] I. Krivenko, https://zenodo.org/record/3930203.
[57] W. F. Brinkman and T. M. Rice, Phys. Rev. B **2**, 4302 (1970).
[58] M. Fabrizio, Phys. Rev. B **76**, 165110 (2007).
[59] J. C. Slater, Phys. Rev. **82**, 538 (1951).